

Fig. 12. Same as Fig. 11, but for $D_{\text{lim}} = 500, 750, 1000,$ and 2000 pc and a different (and still unique) color scale. Superimposed on the first and last maps is the $E(B - V) = 0.1$ iso-contour from the SFD map. $E(B - V) = 0.1$ corresponds the white-to-green transition in the distance-limited opacity maps.

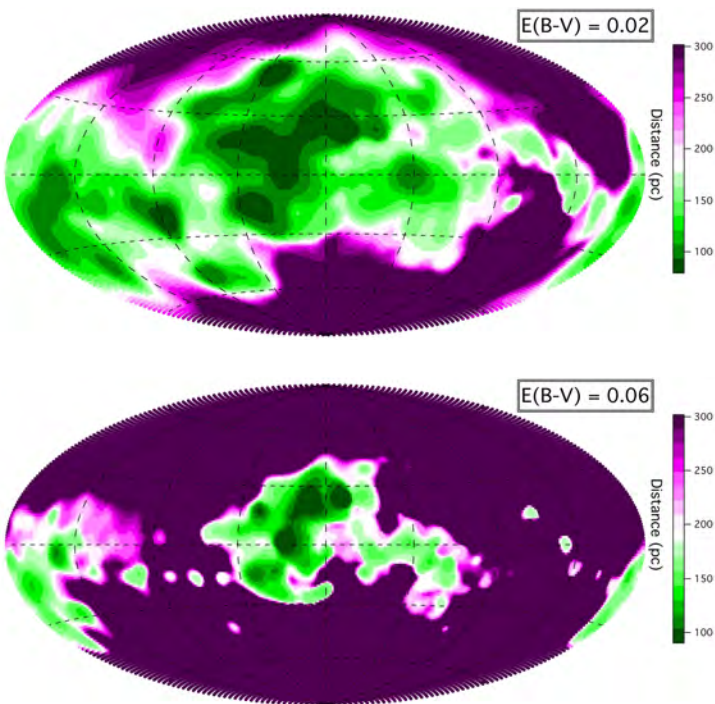


Fig. 13. Distance from the Sun at which the integrated opacity, computed from the inverted differential opacity distribution, is reaching $E(B - V) = 0.02$ mag. Directions corresponding to distances above 300 pc correspond to the purple color. The minimum value (darkest green) is ≈ 80 pc.

Fig. 14. Same as Fig. 13 for $E(B - V) = 0.06$ mag. The minimum value (darkest green) for the distance is ≈ 90 pc.

(biggerbiggercube.u3d)

Fig. 15. Interactive 3D iso-opacity surface for $0.0004 \text{ mag pc}^{-1}$. The Sun is represented by a cube.

transparent surfaces and more structures can be seen at <http://mygepi.obspm.fr/~rlallement/ism3d.html> and <http://mygepi.obspm.fr/~rlallement/ism3dcrevace.html>. However, faint features must be searched for in the slices presented above.

7. Discussion

We have presented new differential opacity maps of the local ISM based on the merging of several photometric catalogs and associated color excess measurements. The data are inverted using a Bayesian code based on the [Tarantola & Valette \(1982\)](#) theoretical work and developed by [Vergely et al. \(2001, 2010\)](#). New spatial correlation kernels were introduced in order to reproduce the ISM structure in a better way, and the quantitative parameters were chosen in a very conservative way to avoid

unrealistic condensations. The maps extend the earlier results of [Vergely et al. \(2010\)](#) to distances of 800–1000 pc at low latitudes and 300 pc below and above the plane.

Our main findings are the following:

- The comparison with the former maps shows good agreement despite using a different reddening database, and different correlation kernels. In particular, the addition of a large number of early-type stars did not affect the Local Cavity boundary mapping. The main clouds are located in 3D space in a way that is coherent with other independent determinations and with 2D dust maps. This demonstrates that the present inversion method gives satisfying results provided parameters are carefully and conservatively chosen in accordance with the number of sightlines entered in the inversion process.

- The combination of the inversion technique and the dataset characteristics is particularly appropriate for revealing nearby interstellar cavities. The geometry and distribution in sizes of those various cavities are available for comparisons with 3D hydrodynamical models of the ISM and bubble evolutions under the repetitive action of stellar winds and supernovae (de Avillez & Breitschwerdt 2009). In particular, the maps reveal a huge cavity that we identify as the superbubble GSH238+00+09 (Heiles 1998) and an elongated cavity in the opposite direction. By giving a global perspective on the distribution of the main clouds and cavities, the new maps may also help shed light on the formation of the Gould belt/Lindblad ring structure, e.g., the scenario devised by Olano (2001) that attributes the formation of the Local arm and the Gould belt to a supercloud having entered a spiral arm 100 Myr ago (see also the recent work of Perrot & Grenier 2003). Indeed, the majority of the cloud complexes seem to surround the chain of cavities formed by GSH238+00+09, the Local Bubble and the $l = 70^\circ$ cavity, and this clearly points to a special role of this $60(70)^\circ$ – $240(250)^\circ$ direction in the local ISM history. We note that this direction is identical to the one of the interstellar helium ionization gradient axis found by Wolff et al. (1999), a potential additional consequence of the event that gave rise to the whole structure.
- The inversion technique and the dataset are also particular appropriate to locating the faint structures that lie above or below the plane ($E(B - V) \leq 0.1$) and are apparent in the emission maps (Schlegel et al. 1998). Such faint and angularly extended clouds cannot be mapped using statistical techniques. The majority of these features are located in 3D and found to be close, at less than ≈ 150 pc. While there is definitely an inclined cavity fully devoid of dust (linking the local *chimneys* to the halo), around this cavity the dust pattern is quite complex. Most faint clouds like the Northern Loop1 arches and the North Celestial Pole Loop are located between 100 and 200 pc.
- The maps can be used to potentially disentangle coincidental similarities in directions for unrelated clouds at different distances. We discussed two particular cases.

We must caution that, in addition to the limitations in spatial resolution, which are linked to the use of a smoothing length, the present dataset is not appropriate for a detailed mapping of the dense clouds. As a matter of fact, there is a limitation in the brightness of the target stars, and the subsequent lack of strongly reddened stars results. This results in a poor representation of regions beyond opaque clouds, because they are badly sampled. There is for the same reasons a bias towards low opacities and some of the opaque clouds are under-represented. Hopefully in future, additional data toward weaker targets will allow those biases to be eliminated, and the decrease in the mean distance between targets will allow using shorter smoothing lengths, leading to better spatial resolution. This is especially mandatory for the dense atomic and molecular phase. This should help for understanding the complex kinematical structure of the whole Sco-Cen area recently derived by Pöppel et al. (2010) based on HI 21 cm data from the Leiden-Dwingeloo Survey and its link with the Gould belt formation. Present or future surveys and especially the Gaia mission should help improving the mapping.

The use of the kinematics that are available from gas emission or absorption data should also help for disentangling the structures and lead to better maps.

Acknowledgements. J.L.V, R.L., and L.P. acknowledge funding by the French Research Agency in the framework of the STILISM project. We thank I. Grenier and J.M. Casandjian for useful discussions, and Matthew Turk from the YT project for helping us with the 3D figure.

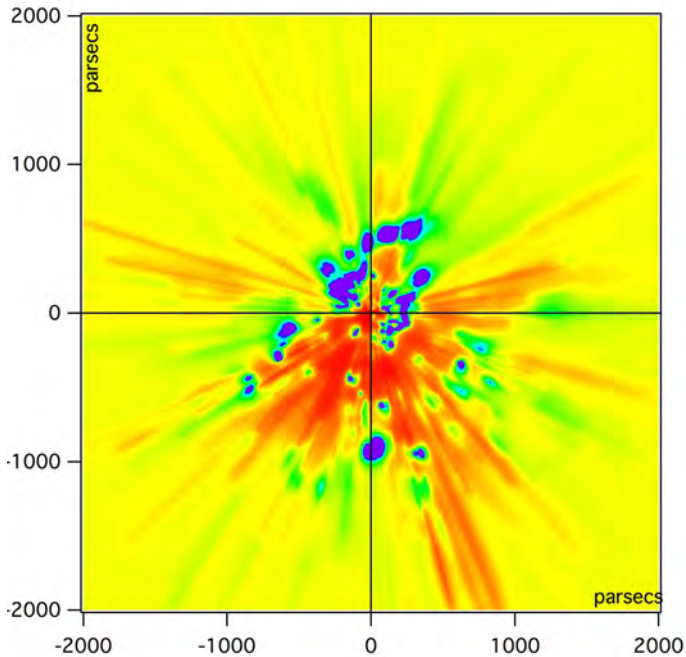
References

- Burningham, B., Naylor, T., Jeffries, R. D., & Devey, C. R. 2003, MNRAS, 346, 1143
- Cambrésy, L., Rho, J., Marshall, D. J., & Reach, W. T. 2011, A&A, 527, A141
- Casagrande, L., Schoenrich, R., Asplund, M., et al. 2011, A&A, 530, A138
- Chen, B., Vergely, J. L., Valette, B., & Carraro, G. 1998, A&A, 336, 137
- Chen, B.-Q., Schultheis, M., Jiang, B. W., et al. 2013, A&A, 550, A42
- Cox, D. P., & Reynolds, R. J. 1987, ARA&A, 25, 303
- Dame, T. M., Ungerechts, H., Cohen, R. S., et al. 1987, ApJ, 322, 706
- de Avillez, M. A., & Breitschwerdt, D. 2009, ApJ, 697, L158
- de Geus, E. J., Bronfman, L., & Thaddeus, P. 1990, A&A, 231, 137
- de Zeeuw, P. T., Hoogerwerf, R., de Bruijne, J. H. J., Brown, A. G. A., & Blaauw, A. 1999, AJ, 117, 354
- Dias, W. S., Alessi, B. S., Moitinho, A., & Lepine, J. R. D. 2012, VizieR Online Data Catalog, II/22
- Dzib, S., Loinard, L., Mioduszewski, A. J., et al. 2010, ApJ, 718, 610
- Cramer, N. 1999, New Astron. Rev., 43, 343
- Gontcharov, G. A. 2012, Astron. Lett., 38, 87
- Grenier, I. A., Lebrun, F., Arnaud, M., Dame, T. M., & Thaddeus, P. 1989, ApJ, 347, 231
- Heiles, C. 1998, ApJ, 498, 689
- Olsen, E. H. 1988, A&A, 189, 173
- Kaltcheva, N., & Makarov, V. 2007, ApJ, 667, L155
- Knude, J. 2010 [arXiv:1006.3676]
- Knude, J. 2011 [arXiv:1103.0455]
- Knude, J., & Lindström, H. E. P. 2012 [arXiv:1202.3600]
- Lallement, R., Welsh, B. Y., Vergely, J. L., Crifo, F., & Sfeir, D. 2003, A&A, 411, 447
- Lilienthal, D., Hirth, W., Mebold, U., & de Boer, K. S. 1992, A&A, 255, 323
- Lombardi, M., Lada, C. J., & Alves, J. 2010, A&A, 512, A67
- Maddalena, R. J., Morris, M., Moscovitz, J., & Thaddeus, P. 1986, ApJ, 303, 375
- Marshall, D. J., Robin, A. C., Reylé, C., Schultheis, M., & Picaud, S. 2006, A&A, 453, 635
- Marshall, D. J., Joncas, G., & Jones, A. P. 2009, ApJ, 706, 727
- Murphy, D. C., & Myers, P. C. 1985, ApJ, 298, 818
- Murphy, D. C., Cohen, R., & May, J. 1986, A&A, 167, 234
- Nordström, B., Mayor, M., Andersen, J., et al. 2004, A&A, 418, 989
- Olano, C. A. 2001, AJ, 121, 295
- Perrot, C. A., & Grenier, I. A. 2003, A&A, 404, 519
- Pöppel, W. G. L., Bajaja, E., Arnal, E. M., & Morras, R. 2010, A&A, 512, A83
- Raimond, S., Lallement, R., Vergely, J.-L., Babusiaux, C., & Eyer, L. 2012 [arXiv:1207.6092]
- Reis, W., Corradi, W., de Avillez, M. A., & Santos, F. P. 2011, ApJ, 734, 8
- Robin, A. C., Reylé, C., Derrière, S., & Picaud, S. 2003, A&A, 409, 523
- Sale, S. E., & Drew, J. E. 2010, Highlights of Astronomy (Berlin: Springer-Verlag), 15, 785
- Schlegel, D. J., Finkbeiner, D. P., & Davis, M. 1998, ApJ, 500, 525 (SFD)
- Serban, D. Z., & Jacobsen, B. H. 2001, Geophys. J. Int., 147, 29
- Straizys, V., Černis, K., & Bartašiūtė, S. 2003, A&A, 405, 585
- Sushch, I., Hnatyk, B., & Neronov, A. 2011, A&A, 525, A154
- Tarantola, A., & Valette, B. 1982, Rev. Geophys. Space Phys., 20, 219
- Turk, M. J., Smith, B. D., Oishi, J. S., et al. 2011, ApJS, 192, 9
- Ungerechts, H., & Thaddeus, P. 1987, ApJS, 63, 645
- van Leeuwen, F. 2007, A&A, 474, 653
- Vergely, J.-L., Freire Ferrero, R., Siebert, A., & Valette, B. 2001, A&A, 366, 1016
- Vergely, J.-L., Valette, B., Lallement, R., & Raimond, S. 2010, A&A, 518, A31
- Welsh, B. Y., Lallement, R., Vergely, J.-L., & Raimond, S. 2010, A&A, 510, A54
- Wolff, B., Koester, D., & Lallement, R. 1999, A&A, 346, 969

Appendix A: Convergence and treatment of oscillations

For most of the choices of parameters, the inversion takes about three to four iteration steps for convergence. We have checked that allowing for more steps does not modify significantly the distribution. The results here were obtained after ten iterations. A number of values for the four main parameters, ξ_0 , ξ_1 , σ_0 , σ_1 were tested. We show here the results for one favored set of parameters. It corresponds to $\xi_0 = 30$ pc, $\sigma_0 = 0.6$, $\xi_1 = 15$ pc, and $\sigma_1 = 0.8$. Our criteria for this choice of parameters are guided by a balance between the quality of the adjustments to the data and a conservative choice of the smoothing lengths. We are also helped by the distribution pattern itself and, in particular, the appearance of elongated radial structures where there are not enough target stars with regard to the used kernel. However, we cannot avoid such radial structures at large distances where targets are missing if we want to keep a kernel appropriate to the nearby regions and uncover the nearby structures. This is illustrated in the Appendix.

Apart from the introduction of new kernels, the updated code now includes a new stage of convergence control. Indeed, in some areas (the problem arose around $l = 80^\circ$ and $b = 0^\circ$, a direction that corresponds to strong changes in the cloud properties with increasing longitude) the correlation length is large compared to the distances, thus the model has difficulties by fitting strong extinctions which are mixed with weak extinctions at distances much shorter than the correlation length. Under these conditions, the model oscillates from one iteration to the other



between the presence of a strong structure of extinction and the absence of extinction: two solutions are then possible for the model. To avoid these oscillations, at the end of the third iteration, one detects the extinction data, which are farther than three sigma from the model. In fact, the model practically converged in the majority of the areas of the Galaxy, except in the significant areas where the gradients in extinction are particularly important. The data that are farther from the model show the areas where the model cannot reach the data. In this case, one increases the variance of the data by a factor of 2; this allows putting less weight on the data that deviate too much from the model. One starts again this filtering with each new iteration. From a practical point of view, about 300 sightlines are thus filtered in third iteration, from the total of 23 000. This number decreases from one iteration to the next and vanishes at the end of the sixth iteration. After convergence, the estimated model privileges smoothed solutions with low extinction values.

Appendix B: Distribution at large distances: constraint limitations

While the inversion was performed in a $4000 \times 4000 \times 600$ pc³, the scarcity of distant stars results in very low or in null constraints beyond ≈ 800 pc. In this case the prior distribution is kept unchanged. We show in Fig. B.1 the computed inverted distribution in the Galactic plane up to + or -2 kpc, in order to illustrate the limits of the area that is actually constrained.

Fig. B.1. Galactic plane cut in the 4000 pc 3D distribution of inverted opacity. This map clearly shows the limits between the prior distribution (homogeneous color) and areas where the model has been constrained by the dataset. The elongated radial structures correspond to directions where cavities over dense areas are detected but the number of target stars is too small to constrain their location, hence the spread over a large distance.

Appendix C: Target distribution

The distribution of the target stars gives the constraints for the inversion. We show in Fig. C.1 those target stars that are located within 10 pc from the plane and have mainly contributed to the computed distribution in this plane, superimposed on the inner part of the computed map. It allows to infer the spatial resolution that can be achieved in a given location. Figure C.2 shows those target stars that are located within 150 pc from the plane and allows to figure out the achievable spatial resolution at larger distance.

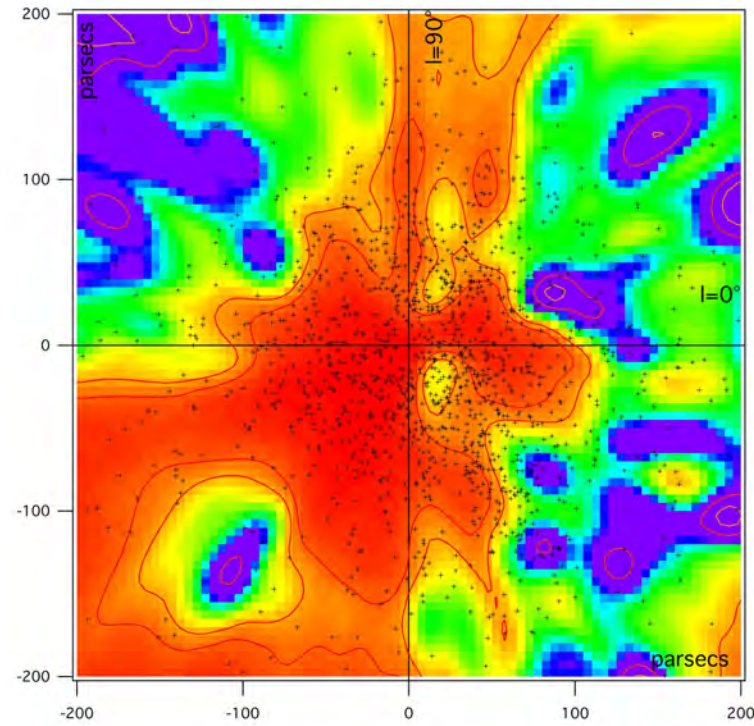


Fig. C.1. The Galactic plane cut in the 3D distribution of inverted opacity with stars within 10 pc from the plane superimposed (plus signs). The distribution shows the regions that are well constrained by the data, and how, given the present limited dataset, nearby cavities are better represented than cloud complexes. The distribution also allows the limiting size for the structures to be figured out from the distance between neighboring targets, on the order of 10 pc in the Sun vicinity.

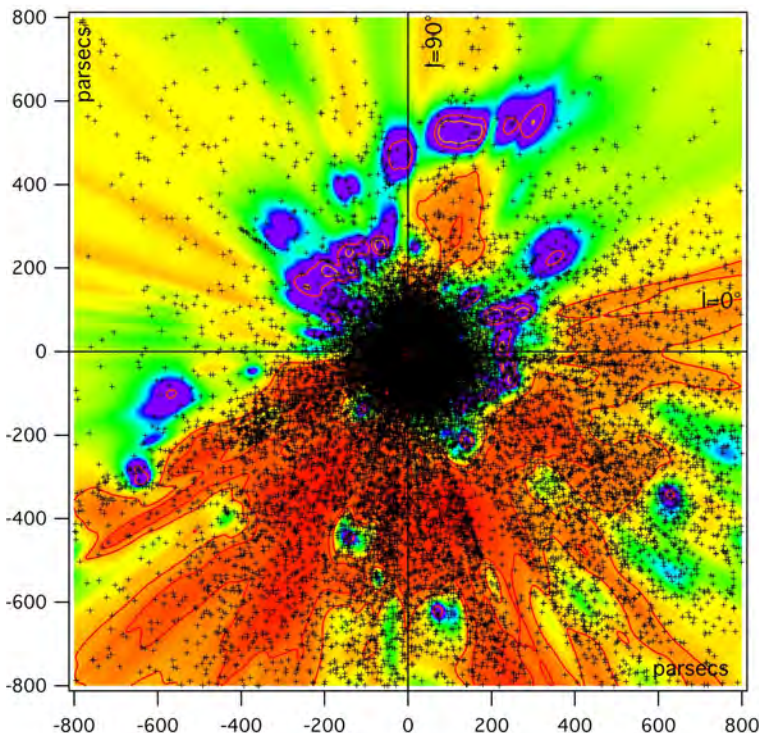


Fig. C.2. Same as Fig. C.1, but extending up to 800 pc and displaying stars within 150 pc from the plane. The limiting size for the inverted structures varies from 40 to 200 pc at 800 pc depending on the regions.